npj | Computational Materials

www.nature.com/npjcompumats

ARTICLE OPEN

Wide-range ideal 2D Rashba electron gas with large spin splitting in $Bi_2Se_3/MoTe_2$ heterostructure

Te-Hsien Wang[1] and Horng-Tay Jeng[1]

An application-expected ideal two-dimensional Rashba electron gas, i.e., nearly all the conduction electrons occupy the Rashba bands, is crucial for semiconductor spintronic applications. We demonstrate that such an ideal two-dimensional Rashba electron gas with a large Rashba splitting can be realized in a topological insulator Bi_2Se_3 ultrathin film grown on a transition metal dichalcogenides $MoTe_2$ substrate through first-principle calculations. Our results show the Rashba bands exclusively over a very large energy interval of about 0.6 eV around the Fermi level within the $MoTe_2$ semiconducting gap. Such a wide-range ideal two-dimensional Rashba electron gas with a large spin splitting, which is desirable for real devices utilizing the Rashba effect, has never been found before. Due to the strong spin–orbit coupling, the strength of the Rashba splitting is comparable with that of the heavy-metal surfaces such as Au and Bi surfaces, giving rise to a spin precession length as small as ~10 nm. The maximum in-plane spin polarization of the inner (outer) Rashba band near the Γ point is about 70% (60%). The room-temperature coherence length is at least several times longer than the spin precession length, providing good coherency through the spin processing devices. The wide energy window for ideal Rashba bands, small spin precession length, as well as long spin coherence length in this two-dimensional topological insulator/transition metal dichalcogenides heterostructure pave the way for realizing an ultrathin nano-scale spintronic device such as the Datta–Das spin transistor at room-temperature.

npj Computational Materials (2017)3:5 ; doi:10.1038/s41524-017-0011-5

INTRODUCTION

The idea of spin field-effect transistor (SFET) proposed by Datta and Das[1] opens up a route to spin information processing.[2] It exploits the Rashba effect, which describes lifting the spin degeneracy of electronic bands through the space inversion asymmetry.[3–5] In a heterojunction without reflection symmetry with respect to the operation $z \rightarrow -z$, z is parallel to the interface normal, the spin–orbit coupling term can be expressed as $H_R = \alpha_R (\mathbf{k} \times \hat{z}) \cdot \sigma$, where σ is the Pauli matrix vector and α_R is the Rashba parameter representing the strength of the Rashba effect. The spin-splitting electronic bands, named Rashba bands (RBs), given from the Hamiltonian diagonalization can be expressed as[6]

$$E_{\pm}(\mathbf{k}) = \frac{\hbar^2 k^2}{2m^*} \pm \alpha_R k, \quad (1)$$

where k is the magnitude of the electron wave vector and m^* the electron effective mass. The in-plane spin polarizations of the "+" and "–" eigenstates are oppositely aligned and normal to the electron wave vector. The Rashba splitting has been observed in many two-dimensional (2D) systems such as the III–V semiconductor heterostructures,[7–9] the metal/semiconductor heterostructures,[10, 11] and the heavy (high-Z) metal films or surfaces.[12–20] The Rashba parameter of the heavy metal systems is generally one order of magnitude larger than that of the III–V semiconductor heterostructures due to the strong spin–orbit coupling of high-Z atoms. For example, the heavy-metal alloy Bi/Ag(111) exhibits a largest Rashba spin splitting of $\alpha_R \approx 3.05$ eVÅ.[17]

For a practical application of these RBs to spintronic devices, two requirements have to be satisfied: (i) a large Rashba splitting and (ii) an ideal Rashba electron gas (REG), i.e., except for the RB states, there is no other electronic states near the Fermi level. A large Rashba splitting mainly comes from the strong spin–orbit coupling of high-Z atoms, which are either metals or semimetals. Therefore, the two requirements, to some extent, are not easily satisfied at the same time. This is the reason why the Datta–Das spin transistor proposed in 1990,[1] which utilizes the Rashba splitting for spin information processing, is finally realized experimentally in 2015.[21] For the III–V semiconductor heterostructures,[7–9] they satisfy the second requirement, but their Rashba splitting is about one order of magnitude smaller than that of the systems composed of high-Z atoms. For the heavy metal surfaces[12–17] and metal thinfilms (quantum well) grown on metal substrates,[18–20] there are always some metal bulk states around the Fermi level. Similar difficulties are also observed in metal/semiconductor junctions[10, 11, 22] as well as in topological insulators.[23–27] Here, we note that the spatial separation between the wave functions of the topological surface states (TSSs) localized on the opposite sides of the Bi_2Se_3 film will deteriorate the performance of the SFET, which is operating through the interference of the wave functions between the two RBs.[1] In the extreme case that the wave functions of the TSSs localized on the opposite sides of the Bi_2Se_3 film are completely separate, the electron spins do not precess because the spin direction of the electrons on each side of the film aligns along the effective magnetic field.[2, 5, 6] To our best knowledge, only the Te-terminated surface of the polar semiconductor BiTeX (X = I, Br, and Cl)[28–30] and the TiO_2-terminated surface of the $SrTiO_3$(001) crystal[31] simultaneously satisfy the two requirements with the

[1]Department of Physics, National Tsing Hua University, Hsinchu 30013, Taiwan
Correspondence: Horng-Tay Jeng (jeng@phys.nthu.edu.tw)

Received: 6 July 2016 Revised: 5 January 2017 Accepted: 16 January 2017
Published online: 09 February 2017

largest Rashba spin splitting of $\alpha_R \approx 3.8$ eVÅ in BiTeI.[28] However the energy interval of the ideal RBs in these bulk-based systems are ~0.25 eV at most.

The 2D materials, such as the V–VI semiconductors M_2N_3 (M = Bi, Sb; N = Te, Se) and the transition metal dichalcogenides XY_2 (X = Mo or W; Y = S, Se, or Te), have attracted tremendous interests in recent years. These materials have been demonstrated its capability to be integrated into electronic devices and open a new perspective in device development.[32, 33] In this work we investigate the electronic structure of a quintuple layer (1QL)-Bi_2Se_3 on a one-trilayer (1TL) $MoTe_2$ through first-principle calculations. As shown in Fig. 1 and will be discussed later, a very good lattice match between the Bi_2Se_3 and the $MoTe_2$ films can be realized in a quite small supercell. We find, in a wide energy range (~0.6 eV), except for the RB states, there is no other electronic states within this $MoTe_2$ semiconducting gap. The Rashba parameter is about one order of magnitude greater than that of the III–V semiconductor heterostructures.[7–9] This is, to our knowledge, the first report of an ideal 2D REG over a very wide energy window with a large Rashba splitting in ultrathin 2D materials. We find the RB states are mainly composed of Bi_2Se_3 orbitals and evolves into the TSSs as the thickness of the Bi_2Se_3 film increases. We also calculate the electronic structures of 1QL-Bi_2Se_3/nTL-$MoTe_2$, n = 1–4, heterostructures, which also exhibit the features of ideal 2D REG and large Rashba splittings. This shows that the RB states are robust and not deteriorated by the presence of a $MoTe_2$ substrate or a $MoTe_2$-terminated substrate. Although we only consider the Bi_2Se_3/$MoTe_2$ heterostructure in this work, similar behavior is expected in some of the other M_2N_3/XY_2 heterostructures.

RESULTS AND DISCUSSION

The band structures of 1QL-Bi_2Se_3/1TL-$MoTe_2$ are shown in Fig. 2. The energy zero is set at the the Fermi level. The Bi_2Se_3 ($MoTe_2$) components and the spin polarizations of the electronic states are represented by the colors of the data points. As can be seen, the RBs are mainly composed of the Bi_2Se_3 orbitals, while the lower energy bands are mainly composed of $MoTe_2$ orbitals. The spin splitting of the RBs induced by the interface electric field extends over a very wide energy interval of ~0.6 eV ranging from ~0.04 eV, the K-point energy of the $MoTe_2$ band, to about 0.67 eV. More importantly, there is no other electronic states within this $MoTe_2$ semiconducting band gap. This wide-range ideal RBs are surely promising for real applications. The Rashba parameter can be approximately estimated by $\alpha_R = 2E_R/k_0$, in which E_R is the Rashba energy and k_0 the wave number offset as indicated in Fig. 3a.[17] In the present case, the deduced Rashba parameter is $\alpha_R = 0.71$ eVÅ, which is about one order of magnitude larger than those of the cases of III–V semiconductor heterostructures $\alpha_R \sim 0.07$ eVÅ,[7–9] and comparable with those of the cases of heavy metals such as Au(111) surface,[12] $\alpha_R \approx 0.36$ eVÅ, and Bi(111) surface,[15] $\alpha_R \approx 0.56$ eVÅ.

In a Datta–Das SFET, when electrons in the channel move a distance d, the electron spins precess by an angle of Δkd, where Δk is the wave number difference (WND) between the two RBs as indicated in Fig. 3a.[1] Therefore the spin flips when the electron wave propagates over the precession length $L = \pi/\Delta k$. As shown in Fig. 3b, the WND Δk decreases monotonically with increasing energy, while the spin precession length L increases approximately linearly with energy. Due to the strong spin–orbit coupling, the strength of the Rashba splitting is comparable with that of the heavy-metal surfaces such as Au and Bi surfaces, giving rise to a spin precession length as small as 10 nm. In comparison with the micrometer scale Datta–Das spin transistor realized in 2015,[21] the large spin splitting and small precession length in this ultrathin 1QL-Bi_2Se_3/1TL-$MoTe_2$ heterostructure pave the way to achieve the spintronic device at the nanoscale. Similar behavior is also expected in different ultrathin TI/TMD heterostructures, providing high flexibility for real applications.

For the ideal 2DEG model, the RBs are perfectly parabolic as shown in Eq. (1). Since the WND and the spin precession length L are energy-independent, or equivalently the Rashba spin splitting is linear-in-k, all the electron spins precess coherently by the same angle during transport. However, in practical cases, the Rashba band dispersion deviates from the ideal parabolic form, the WND as well as the spin precession length are thus energy-dependent. This will cause spin precession incoherency of the electric current

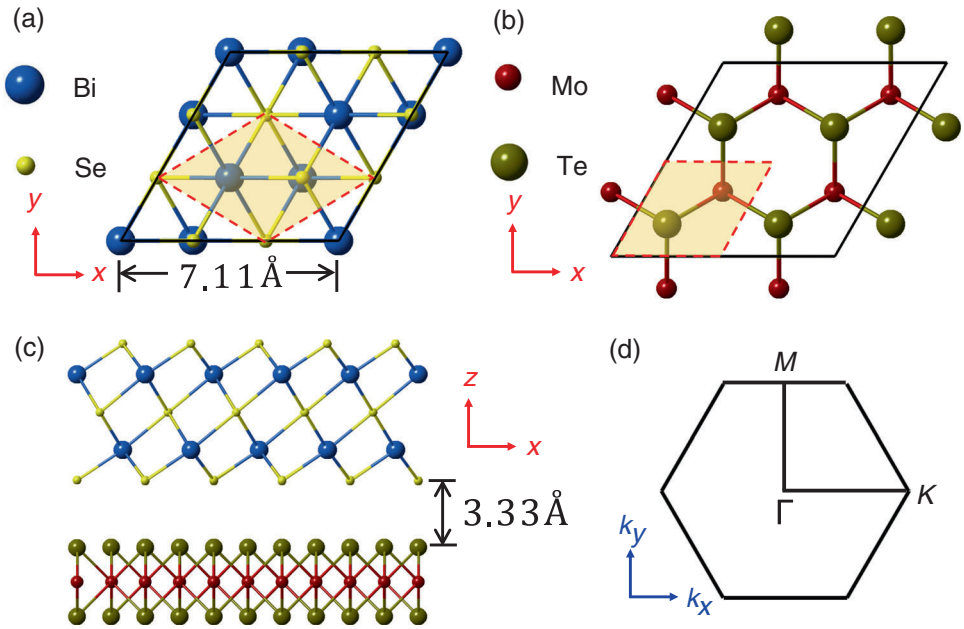

Fig. 1 The optimized lattice of the 1QL-Bi_2Se_3/1TL-$MoTe_2$ heterostructure. **a** *Top view* of the Bi_2Se_3 part. **b** *Top view* of the $MoTe_2$ part. **c** *Side view* of the whole system. The supercell used in the calculations is denoted in **a** and **b** by the *black solid line*, in which the Bi_2Se_3-$(\sqrt{3}\times\sqrt{3})R30°$/$MoTe_2$-(2 × 2) system is incorporated. The shaded regions in **a** and **b** denote, respectively, the Bi_2Se_3 and the $MoTe_2$ 1 × 1 unit cell. The corresponding Brillouin zone is shown in (**d**)

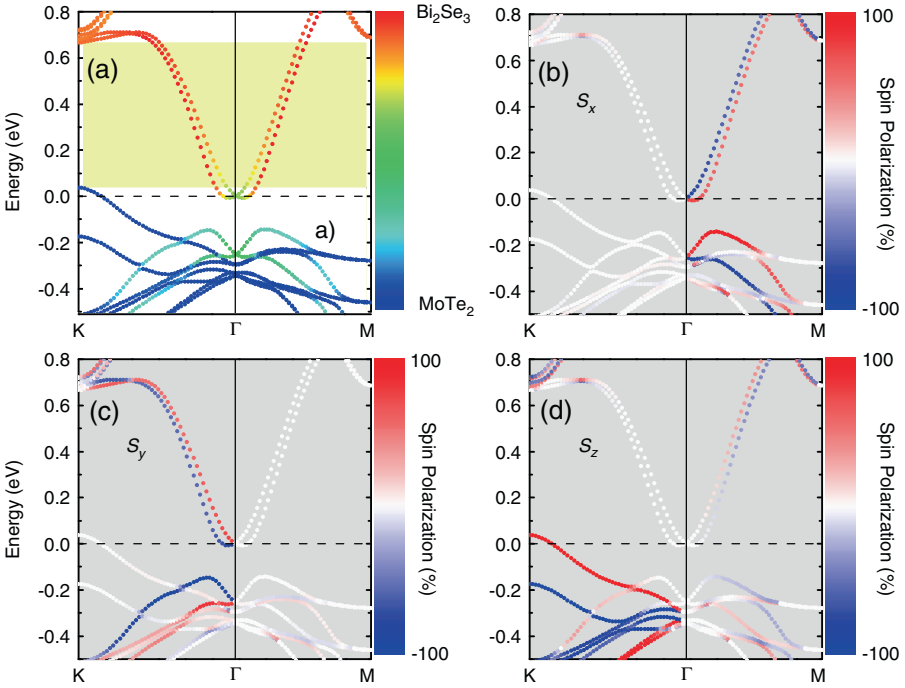

Fig. 2 Electronic structures of the 1QL-Bi_2Se_3/1TL-$MoTe_2$ junction, where **a** the Bi_2Se_3 and the $MoTe_2$ components, **b**–**d** spin polarization along the *x*, *y* and *z* directions are represented by the *color* of the *dots*. The *yellow-shaded* region in **a** indicates the energy window (over 0.6 eV) for ideal Rashba bands without any other electronic states

in a SFET and make the device ineffective. The ideal Rashba dispersion shown in Eq. 1 has two features, the linear-in-k Rashba spin splitting and the energy-independent WND. It would be more meaningful to investigate the deviation from the energy-independent WND than the deviation from the linear-in-k Rashba spin splitting because the Datta–Das transistor is operating through the wave-function interference between the two RB states of the same energy with different wave numbers.[1] To quantitatively describe the spin coherency of conduction electrons, which mainly distribute over the thermal energy range k_BT around the Fermi level, we define the coherence length l_c as

$$l_c(E,T) = \left| \frac{1}{\Delta k(E) - \Delta k(E + k_BT)} \right|. \quad (2)$$

The coherence length l_c is the electron propagation distance over which the difference of the precession angles between any two electrons within the energy range k_BT is smaller than unity, i.e., 57°. Here, for simplicity, we assume the magnitude of Δk varies monotonically with energy in an energy range k_BT. The room-temperature ($k_BT = 25.9$ meV) coherence length l_c obtained by Eq. (2) and the ratio of the l_c to the spin precession length L are plotted in the inset of Fig. 3b. As can be seen, the coherence length is about 0.1 μm, and at least several times larger than the spin precession length of about 10 nm, guaranteeing the coherency of all the electrons transporting over the precession length.

The *x*, *y*, and *z* components of spin polarization are shown in Fig. 2b, c, and d, in which the Γ–K direction is along the *x* direction and the Γ–M direction along the *y* direction as indicated in Fig. 1. For a free-standing Bi_2Se_3 film, the crystal structure has inversion symmetry and belongs to $P\bar{3}m1$ (D_{3d}^3) space group. When the $MoTe_2$ film is incorporated, i.e., Bi_2Se_3/$MoTe_2$ heterostructure, the symmetry is reduced to $P3$ (C_3^1) with broken inversion symmetry. As a result, the spin degeneracies of the Bi_2Se_3 branches are lifted, forming the conduction Bi_2Se_3 RBs with helical spin polarizations as evidenced by Fig. 2b and c. While the out-of-plane spin polarizations of the RBs in Fig. 2d are nearly zero around the Γ point and otherwise increases due to the warping effect. As for the top valence bands given from the 1TL-$MoTe_2$, the band dispersion as well as the spin polarization (Fig. 2) are similar to the standard free standing transition-metal dichalcogenides cases.[34]

The spin texture of the RBs of energies 0.1, 0.3, and 0.5 eV is shown in Fig. 4a. The band dispersion is nearly isotropic below ~0.3 eV, and it exhibits significant hexagonal warping around 0.5 eV. The in-plane spin polarization (arrow) of the inner RB and the outer RB circulates the energy contour oppositely, keeping the overall time-reversal symmetry. While the out-of-plane spin polarization (color of the arrow) warps within ±30% with zero values at *K* points due to the reflection symmetry about the *x*–*z* plane in the Bi_2Se_3 layer. As shown in Fig. 4b, the magnitude of the in-plane spin polarization (solid line) is nearly a constant for electrons of the same energy (in between the dotted lines), and much greater than that of the azimuthal average of the out-of-plane spin polarization (dashed line). For the inner (outer) RB near the Γ point, the maximum values is about 70% (60%), which is comparable with that of the Bi_2Se_3 TSSs reported in refs. 35 and 36. It decreases slowly to about 50% as the energy increases to 0.5 eV. These less-than-unity spin polarization is due to the spin–orbit entanglement, by which the spin polarization contributed from different orbitals could cancel each other.[35, 36]

Figure 5a shows the optimized lattice structure of the 2QL-Bi_2Se_3/1TL-$MoTe_2$ heterostructure, in which the two Bi_2Se_3 QLs stack in the usual ABC fashion. Bi_2Se_3 is theoretically predicted[37, 38] and experimentally observed[37, 39] to be a three-dimensional topological insulator with a single Dirac cone. Therefore, through increasing the Bi_2Se_3 thickness, we can find the Dirac-like surface states as shown in Fig. 5b, in which there are two Dirac cones with the Dirac points at energies −29 and −212 meV. The two Dirac cones correspond to surface states on the interface side and the surface side of the Bi_2Se_3 film.[27, 40] The higher energy interface Dirac state (inner RB) shows strong hybridization between the Bi_2Se_3 and the $MoTe_2$ orbitals. While the lower energy surface Dirac state (outer RB) is mainly composed of the Bi_2Se_3 orbitals. Due to the finite size effect,[41, 42]

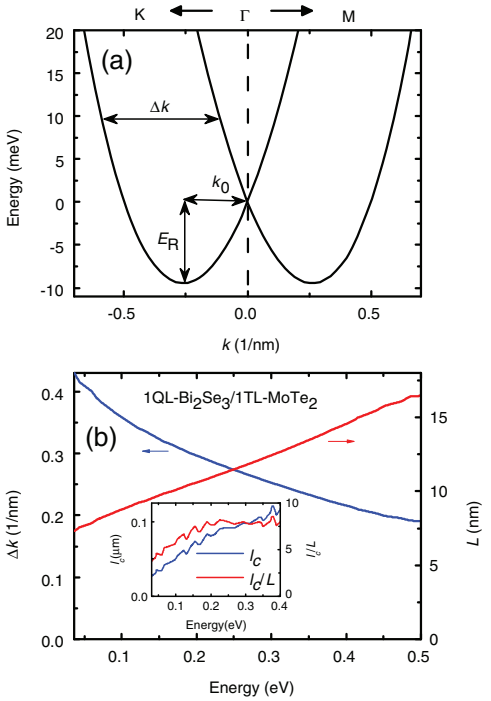

Fig. 3 **a** The zoom-in of the electronic structure of the 1QL-Bi_2Se_3/1TL-$MoTe_2$ heterostructure near the Γ point. The Rashba energy E_R, the wave number offset k_0, and the WND between the two RBs Δk are indicated. **b** The WND between the two RBs Δk and the corresponding spin precession length L as functions of energy. The *inset* shows the coherence length l_c and the ratio of the l_c to the spin precession length as functions of energy

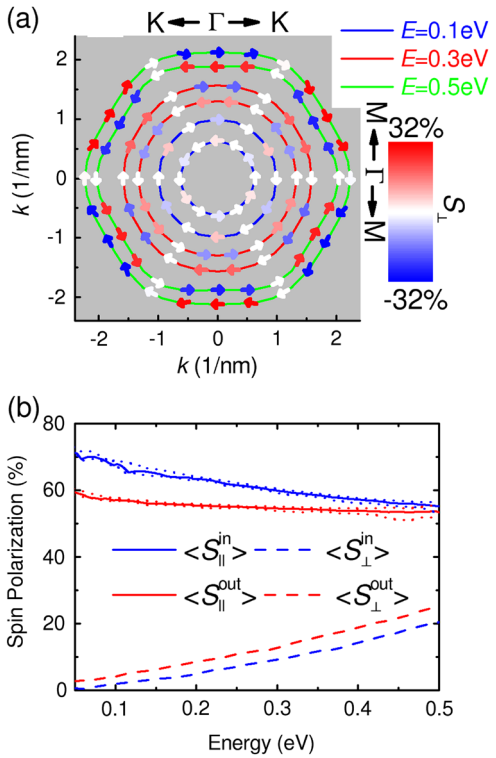

Fig. 4 **a** Spin texture of the 1QL-Bi_2Se_3/1TL-$MoTe_2$ heterostructure. The in-plane spin-polarization directions $S_{\parallel}$ are indicated by the *arrows*. The out-of-plane spin polarizations $S_{\perp}$ are represented by the *color* of the *arrows*. **b** The azimuthal average of the magnitude of the spin polarization. The *blue* (*red*) lines are those of the *inner* (*outer*) Rashba branch, and the *solid* (*dashed*) *lines* are those of the in-plane (out-of-plane) component. The maximum and minimum magnitudes of the in-plane spin polarization are indicated by the *dotted lines*

the coupling between the interface states and the surface states opens a small gap of ~30 meV. For a thicker Bi_2Se_3 film (≥6QL), the interface states and the surface states evolve into gapless and spatially separate TSSs. This would cause the SFET losing its ability to modulate the electric current because each of the surface and interface states has electron spin aligned with the effective magnetic field on different side of the Bi_2Se_3 film. Further details about the thickness dependence and the charge density profiles of the RBs can be found in S6 of the Supplementary Information. Moreover additional Bi_2Se_3 QWSs emerge with band edge at 238 meV due to the increasing film thickness. Further restricted by the $MoTe_2$ valence band maximum of 38 meV at *K*, the energy range of the ideal 2D REG is suppressed to only ~0.2 eV. Similar features (i.e., the Dirac cones and the QWSs) can be found in 3QL-Bi_2Se_3/1TL-$MoTe_2$ and 2QL-Bi_2Se_3/2TL-$MoTe_2$ heterostructures as shown in Figure S3 of the Supplementary Information. Figure 5c shows the corresponding WND and the spin precession length as functions of energy where the unshaded region indicate the energy range of the ideal 2D REG. They are comparable with those of 1QL-Bi_2Se_3/1TL-$MoTe_2$. The inset shows the room-temperature coherence length. In the energy region from 0.16 to 0.21 eV, the coherence length is more than 50 times longer than the spin precession length.

To investigate the substrate effect, we consider the case of 1QL-Bi_2Se_3/2TL-$MoTe_2$. The optimized structure is illustrated in Fig. 5d, in which the two $MoTe_2$ TLs are in the 2*H* stacking sequence. Shown in Fig. 5e, the $MoTe_2$ band at Γ is higher than that at *K* and is 123 meV higher than the RB minimum. Similar valence-band maximum shift from *K* to Γ upon increasing TMD film thickness has been reported.[43] The resultant energy window for the ideal RBs, the spin precession length, as well as the coherence length remain comparable with those of the 1QL-Bi_2Se_3/1TL-$MoTe_2$ case. We also carry out similar calculations for 1QL-Bi_2Se_3/3TL-$MoTe_2$ and 1QL-Bi_2Se_3/4TL-$MoTe_2$ (see Supporting Information Fig. S1) and obtain similar results. This indicates that these RBs are robust and nearly free from the influence of the substrate if the 1QL-Bi_2Se_3 film is grown on the $MoTe_2$ or $MoTe_2$-terminated substrate.

In summary, we demonstrate that ideal 2D REG can be established in a 1QL-Bi_2Se_3 film grown on the $MoTe_2$ or $MoTe_2$-terminated substrate. Our calculations show a very wide energy range (~0.6 eV) for the TI-RBs exclusively around the Fermi level within the TMD semiconducting gap. The large spin splitting in the RBs is comparable with that of other heavy metal surface states, leading to a spin precession length as small as ~10 nm. The maximum in-plane spin polarization is about 70% (60%) for the inner (outer) RB, similar to the typical TI ones. For 1QL-Bi_2Se_3/*n*TL-$MoTe_2$, $n = 1$–4 studied in this work, we find the RBs very robust against the variation of the thickness of the $MoTe_2$ film. While increasing Bi_2Se_3 film thickness would suppress the energy window of the ideal REG and the performance of the SFET. The room-temperature coherence length of all the systems studied in this work is at least several times longer than the spin precession length. Thus the REG in our proposed ultrathin TI/TMD heterostructure will propagate coherently over the spin precession length, achieving the room-temperature 2D Datta–Das spin transistor at the nano-scale.

METHODS

The calculations are performed in the framework of density functional theory by using Vienna ab-initio simulation package with the Perdew-

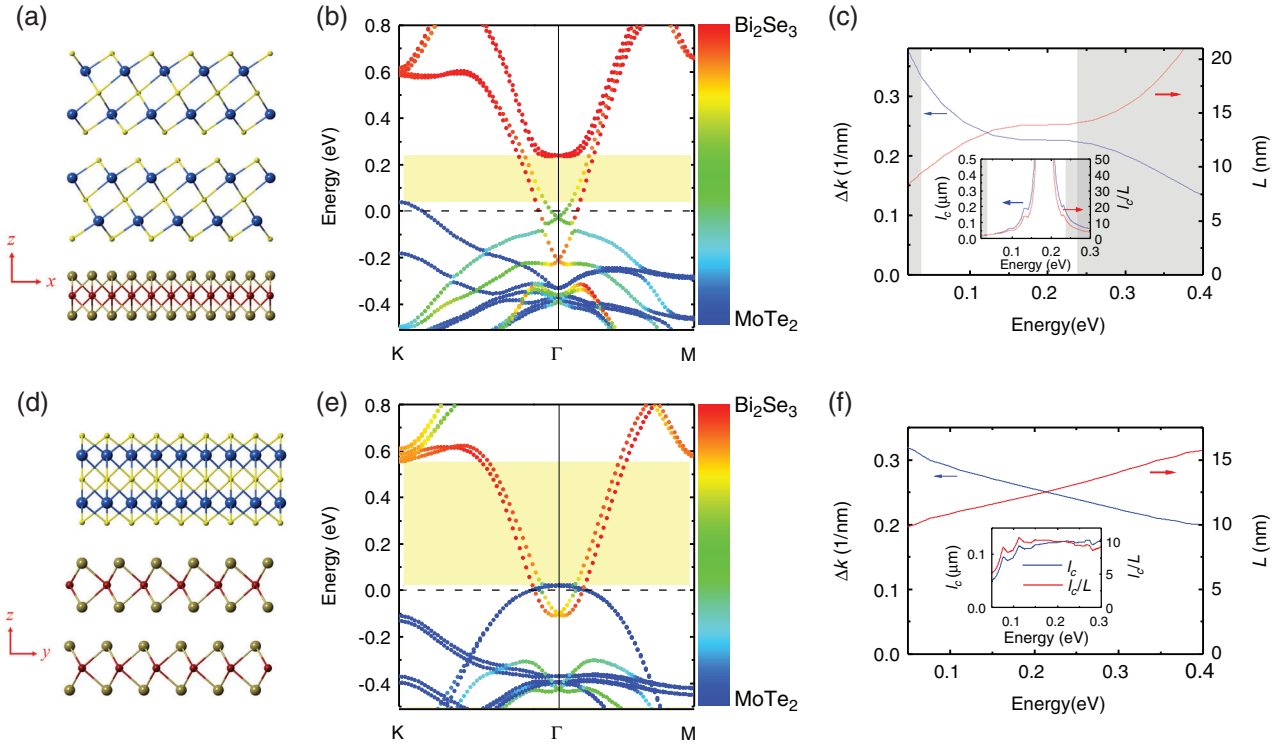

Fig. 5 **a** Side view of the 2QL-Bi_2Se_3/1TL-$MoTe_2$ heterostructure. **b** Band structures of the 2QL-Bi_2Se_3/1TL-$MoTe_2$. The Bi_2Se_3 and the $MoTe_2$ components are represented by the *color* of the *dots*. The *yellow-shaded* region indicates the energy region for ideal RB states. **c** The WND between the two RBs Δk of the 2QL-Bi_2Se_3/1TL-$MoTe_2$ heterostructure and the corresponding spin precession length L as functions of energy. The *inset* shows the coherence length l_c and the ratio of the l_c to the spin precession length as functions of energy. The *shaded* regions indicate the energy regions where the other states (high-energy quantum well states or the $MoTe_2$ states near the K point) are involved. **d**–**f** are the counterparts of **a**–**c**, respectively, for the case of the 1QL-Bi_2Se_3/2TL-$MoTe_2$ heterostructure

Burke-Ernzerhof generalized gradient approximation.[44–46] The electron ion interaction is described by projected augmented wave potentials.[47] The spin–orbit coupling is taken into account. Because of the lattice mismatch between the Bi_2Se_3 and $MoTe_2$ films, we adopt supercell calculations. As shown in Fig. 1, the supercell contains 1QL of Bi_2Se_3-$(\sqrt{3}\times\sqrt{3})$ $R30°$ and 1TL of $MoTe_2$-(2×2). The resulting lattice mismatch is 2%. A $7\times7\times1$ Γ-centered Monkhorst-Pack k-mesh is used for the integration of Brillouin zone.[48] The cutoff energy for plane wave basis is set as 400 eV. All of the atomic positions as well as the lattice are fully relaxed until the magnitude of the force acting on all atoms is less than 0.005 eVÅ^{-1} and the total energy converges within 10^{-7} eV. The van der Waals interactions based on the DFT-D3 method with Becke-Jonson damping[49, 50] are included in the structure relaxation. The optimized interlayer spacing between the Bi_2Se_3 and the $MoTe_2$ layer is 3.33 Å.

ACKNOWLEDGEMENTS

This work was supported by the Ministry of Science and Technology, Taiwan. H.T.J. also thanks NCHC, CINC-NTU, and NCTS, Taiwan for technical support.

AUTHOR CONTRIBUTIONS

T. H. W performed the calculations, analyzed the data, and wrote the manuscript. H. T. J. conceived and supervised the project. All authors reviewed the manuscript.

COMPETING INTERESTS

The authors declare no competing interests.

REFERENCES

1. Datta, S. & Das, B. Electronic analog of the electrooptic modulator. *Appl. Phys. Lett.* **56**, 665–667 (1990).
2. Zutic, I., Fabian, J. & Das Sarma, S. Spintronics: fundamentals and applications. *Rev. Mod. Phys.* **76**, 323–410 (2004).
3. Rashba, E. I. Properties of semiconductors with an extremum loop.1. Cyclotron and combinational resonance in a magnetic rield perpendicular to the plane of the loop. *Sov. Phys.Sol. State* **2**, 1109–1122 (1960).
4. Bychkov, Y. A. & Rashba, E. I. Properties of a 2D electron-gas with lifted spectral degeneracy. *JEPT Lett* **39**, 78–81 (1984).
5. Manchon, A., Koo, H. C., Nitta, J., Frolov, S. M. & Duine, R. A. New perspectives for Rashba spin–orbit coupling. *Nat. Mater.* **14**, 871–882 (2015).
6. Okuda, T. & Kimura, A. Spin- and angle-resolved photoemission of strongly spin–orbit coupled systems. *J. Phys. Soc. Jpn* **82**, 021002 (2013).
7. Luo, J., Munekata, H., Fang, F. F. & Stiles, P. J. Effects of inversion asymmetry on electron-energy band structures in GaSb/InAs/GaSb quantum-wells. *Phys. Rev. B* **41**, 7685–7693 (1990).
8. Das, B., Miller, D. C., Datta, S., Reifenberger, R., Hong, W. P., Bhattacharya, P. K., Singh, J. & Jaffe, M. Evidence for spin splitting in $In_xGa_{1-x}As/In_{0.52}Al_{0.48}As$ heterostructures as B→0. *Phys. Rev. B* **39**, 1411–1414 (1989).
9. Nitta, J., Akazaki, T., Takayanagi, H. & Enoki, T. Gate control of spin–orbit interaction in an inverted $In_{0.53}Ga_{0.47}As/In_{0.52}Al_{0.48}As$ heterostructure. *Phys. Rev. Lett.* **78**, 1335–1338 (1997).
10. Dil, J. H. *et al.* Rashba-type spin–orbit splitting of quantum well states in ultrathin Pb films. *Phys. Rev. Lett.* **101**, 266802 (2008).
11. Yaji, K. *et al.* Large Rashba spin splitting of a metallic surface-state band on a semiconductor surface. *Nat. Commun.* **1**, 17 (2010).
12. LaShell, S., McDougall, B. A. & Jensen, E. Spin splitting of an Au(111) surface state band observed with angle resolved photoelectron spectroscopy. *Phys. Rev. Lett.* **77**, 3419–3422 (1996).
13. Hochstrasser, M., Tobin, J. G., Rotenberg, E. & Kevan, S. D. Spin-resolved photoemission of surface states of W(110)-(1×1)H. *Phys. Rev. Lett.* **89**, 216802 (2002).
14. Hoesch, M. *et al.* Spin structure of the Shockley surface state on Au(111). *Phys. Rev. B* **69**, 241401 (2004).
15. Koroteev, Y. M. *et al.* Strong spin–orbit splitting on Bi surfaces. *Phys. Rev. Lett.* **93**, 046403 (2004).
16. Varykhalov, A. *et al.* Ir(111) surface state with giant Rashba splitting persists under graphene in air. *Phys. Rev. Lett.* **108**, 066804 (2012).

17. Ast, C. R. *et al.* Giant spin splitting through surface alloying. *Phys. Rev. Lett.* **98**, 186807 (2007).
18. Varykhalov, A. *et al.* Quantum cavity for spin due to spin-orbit interaction at a metal boundary. *Phys. Rev. Lett.* **101**, 256601 (2008).
19. Shikin, A. M. *et al.* Origin of spin–orbit splitting for monolayers of Au and Ag on W (110) and Mo(110). *Phys. Rev. Lett.* **100**, 057601 (2008).
20. Mathias, S. *et al.* Quantum-well-induced giant spin-orbit splitting. *Phys. Rev. Lett.* **104**, 066802 (2010).
21. Chuang, P. *et al.* All-electric all-semiconductor spin field-effect transistors. *Nat. Nanotechnol* **10**, 35–39 (2015).
22. Ming, W., Wang, Z. F., Zhou, M., Yoon, M. & Liu, F. Formation of ideal Rashba states on layered semiconductor surfaces steered by strain engineering. *Nano Letters* **16**, 404–409 (2016).
23. King, P. D. C. *et al.* Large tunable Rashba spin splitting of a two-dimensional electron gas in Bi_2Se_3. *Phys. Rev. Lett.* **107**, 096802 (2011).
24. Valla, T., Pan, Z. H., Gardner, D., Lee, Y. S. & Chu, S. Photoemission spectroscopy of magnetic and nonmagnetic impurities on the surface of the Bi_2Se_3 topological insulator. *Phys. Rev. Lett.* **108**, 117601 (2012).
25. Bianchi, M., Hatch, R. C., Mi, J. L., Iversen, B. B. & Hofmann, P. Simultaneous quantization of bulk conduction and valence states through adsorption of nonmagnetic impurities on Bi_2Se_3. *Phys. Rev. Lett.* **107**, 086802 (2011).
26. Benia, H. M., Lin, C. T., Kern, K. & Ast, C. R. Reactive chemical doping of the Bi_2Se_2 topological insulator. *Phys. Rev. Lett.* **107**, 177602 (2011).
27. Zhang, Y. *et al.* Crossover of the three-dimensional topological insulator Bi_2Se_3 to the two-dimensional limit. *Nat. Phys* **6**, 584–588 (2010).
28. Ishizaka, K. *et al.* Giant Rashba-type spin splitting in bulk BiTeI. *Nat. Mater* **10**, 521 (2011).
29. Eremeev, S. V., Nechaev, I. A., Koroteev, Y. M., Echenique, P. M. & Chulkov, E. V. Ideal two-dimensional electron systems with a giant Rashba-type spin splitting in real materials: surfaces of bismuth tellurohalides. *Phys. Rev. Lett.* **108**, 246802 (2012).
30. Sakano, M. *et al.* Strongly spin–orbit coupled two-dimensional electron gas emerging near the surface of polar semiconductors. *Phys. Rev. Lett.* **110**, 107204 (2013).
31. Santander-Syro, A. F. *et al.* Giant spin splitting of the two-dimensional electron gas at the surface of $SrTiO_3$. *Nat. Mater.* **13**, 1085–1090 (2014).
32. Wang, Q. H., Kalantar-Zadeh, K., Kis, A., Coleman, J. N. & Strano, M. S. Electronics and optoelectronics of two-dimensional transition metal dichalcogenides. *Nat. Nanotechnol* **7**, 699–712 (2012).
33. Fiori, G. *et al.* Electronics based on two-dimensional materials. *Nat. Nanotechnol* **9**, 768–779 (2014).
34. Zhu, Z. Y., Cheng, Y. C. & Schwingenschlogl, U. Giant spin–orbit-induced spin splitting in two-dimensional transition-metal dichalcogenide semiconductors. *Phys. Rev. B* **84**, 153402 (2011).
35. Yazyev, O. V., Moore, J. E. & Louie, S. G. Spin polarization and transport of surface states in the topological insulators Bi_2Se_3 and Bi_2Te_3 from first principles. *Phys. Rev. Lett.* **105**, 266806 (2010).
36. Zhu, Z. H. *et al.* Layer-by-layer entangled spin–orbital texture of the topological surface state in Bi_2Se_3. *Phys. Rev. Lett.* **110**, 216401 (2013).
37. Xia, Y. *et al.* Observation of a large-gap topological-insulator class with a single Dirac cone on the surface. *Nat. Phys* **5**, 398–402 (2009).
38. Zhang, H. J. *et al.* Topological insulators in Bi_2Se_3, Bi_2Te_3 and Sb_2Te_3 with a single Dirac cone on the surface. *Nat. Phys* **5**, 438–442 (2009).
39. Hsieh, D. *et al.* A tunable topological insulator in the spin helical Dirac transport regime. *Nature* **460**, 1101–1105 (2009).
40. Shan, W. Y., Lu, H. Z. & Shen, S. Q. Effective continuous model for surface states and thin films of three-dimensional topological insulators. *New J. Phys.* **12**, 043048 (2010).
41. Zhou, B., Lu, H. Z., Chu, R. L., Shen, S. Q. & Niu, Q. Finite size effects on helical edge states in a quantum spin-hall system. *Phys. Rev. Lett.* **101**, 246807 (2008).
42. Linder, J., Yokoyama, T. & Sudbo, A. Anomalous finite size effects on surface states in the topological insulator Bi_2Se_3. *Phys. Rev. B* **80**, 205401 (2009).
43. Kuc, A., Zibouche, N. & Heine, T. Influence of quantum confinement on the electronic structure of the transition metal sulfide TS_2. *Phys. Rev. B* **83**, 245213 (2011).
44. Perdew, J. P., Burke, K. & Ernzerhof, M. Generalized gradient approximation made simple. *Phys. Rev. Lett.* **77**, 3865–3868 (1996).
45. Kresse, G. & Furthmuller, J. Efficiency of ab-initio total energy calculations for metals and semiconductors using a plane-wave basis set. *Comput. Mater. Sci* **6**, 15–50 (1996).
46. Kresse, G. & Furthmuller, J. Efficient iterative schemes for ab initio total-energy calculations using a plane-wave basis set. *Phys. Rev. B* **54**, 11169–11186 (1996).
47. Blochl, P. E. Projector augmented-wave method. *Phys. Rev. B* **50**, 17953–17979 (1994).
48. Monkhorst, H. J. & Pack, J. D. Special points for Brillouin-zone integrations. *Phys. Rev. B* **13**, 5188 (1976).
49. Grimme, S., Antony, J., Ehrlich, S. & Krieg, H. A consistent and accurate ab initio parametrization of density functional dispersion correction (DFT-D) for the 94 elements H-Pu. *J. Chem. Phys.* **132**, 154104 (2010).
50. Grimme, S., Ehrlich, S. & Goerigk, L. Effect of the damping function in dispersion corrected density functional theory. *J. Comput. Chem.* **32**, 1456–1465 (2011).

Supplementary Information accompanies the paper on the *npj Computational Materials* website (doi:10.1038/s41524-017-0011-5).